Local structure of the metal–oxygen bond in compositionally homogeneous, nanocrystalline zirconia–ceria solid solutions synthesized by a gel-combustion process

2006 J. Phys.: Condens. Matter 18 7863

(http://iopscience.iop.org/0953-8984/18/34/002)

INSTITUTE OF PHYSICS PUBLISHING JOURNAL OF PHYSICS: CONDENSED MATTER

J. Phys.: Condens. Matter **18** (2006) 7863–7881 doi:10.1088/0953-8984/18/34/002

Local structure of the metal–oxygen bond in compositionally homogeneous, nanocrystalline zirconia–ceria solid solutions synthesized by a gel-combustion process

Ismael O Fábregas[1], Rodolfo O Fuentes[1], Diego G Lamas[1], María E Fernández de Rapp[1], Noemí E Walsöe de Reca[1], Marcia C A Fantini[2], Aldo F Craievich[2], Rogério Junqueira Prado[3], Ricardo P Millen[4] and Marcia L A Temperini[4]

[1] CINSO (Centro de Investigaciones en Sólidos), CITEFA-CONICET, J.B. de La Salle 4397, (1603) Villa Martelli, Provincia de Buenos Aires, Argentina
[2] Instituto de Física, Universidade de São Paulo, Travessa R da Rua do Matão, no.187, Cidade Universitária, 05508-900, São Paulo, Brazil
[3] Departamento de Recursos Minerais (DRM-ICET), Universidade Federal de Mato Grosso (UFMT), Avenida Fernando Corrêa s/n, 78060-900, Cuiabá-MT, Brazil
[4] Instituto de Química, Universidade de São Paulo, Avenida Prof. Lineu Prestes 748, Cidade Universitaria, 05508-900, São Paulo, Brazil

E-mail: dlamas@citefa.gov.ar

Received 19 May 2006, in final form 12 July 2006
Published 7 August 2006
Online at stacks.iop.org/JPhysCM/18/7863

Abstract

Compositionally homogeneous ZrO_2–CeO_2 nanopowders have been characterized by Raman and extended x-ray absorption fine structure (EXAFS) spectroscopies. These techniques revealed a tetragonal-to-cubic phase transition as a function of CeO_2 content, as observed in a previous synchrotron x-ray diffraction study. The tetragonal–cubic phase boundary was found to be at (85 ± 5) mol% CeO_2. The EXAFS study demonstrated that this transition is related to a tetragonal-to-cubic symmetry change of the Zr–O first neighbour coordination sphere, while the Ce–O coordination sphere preserves its cubic symmetry over the whole composition range.

1. Introduction

ZrO_2–CeO_2 substitutional solid solutions are extensively used as redox or oxygen storage promoters in three-way catalysts, which are applied in controlling the emissions of NO_x, CO and hydrocarbons from automotive exhausts [1]. The properties of ZrO_2–CeO_2 mixed oxides are strongly related to their crystal structure and local order [1, 2]. In particular, the metastable

forms of the tetragonal phase have been widely investigated since they are the most suitable for applications [1].

The crystal structure of compositionally homogeneous ZrO_2–CeO_2 solid solutions has been studied by Yashima *et al* [3–6]. These authors have investigated a number of materials synthesized by the solid-state reaction method. They reported the existence of three forms of the tetragonal phase, all belonging to the $P4_2/nmc$ space group. The stable form of the tetragonal phase is called the t form, which is restricted to the solubility limit predicted by the equilibrium phase diagram [7]. The t' form has a wider solubility range, but it is unstable, the stable phase in this compositional range being a mixture of the t-form and the cubic phase. Finally, the t'' form has an axial ratio c/a equal to unity, but with the oxygen ions displaced from their ideal sites of the cubic structure (8c sites of the $Fm\bar{3}m$ space group) along the c axis. The t'/t'' and t''/c boundaries reported by Yashima *et al* were of 60 and 85 mol% CeO_2, respectively [6].

Materials prepared by using the solid-state reaction method, as those studied by Yashima and co-authors, are composed of rather large crystals with an average size typically above a micrometre. Later, several authors demonstrated that nanocrystalline, compositionally homogeneous ZrO_2–CeO_2 materials exhibit the same metastable forms as the tetragonal phase [8–12]. However, these authors found difficulties in discriminating between the t' and t'' forms of the tetragonal phase and between the t'' form and the cubic phase. In addition, it should be pointed out that several discrepancies and misunderstandings can be observed in these works [8–12].

The local structure of the metal–oxygen bond in compositional homogeneous ZrO_2–CeO_2 solid solutions has been investigated by EXAFS by several authors [13–19]. Even though there is a general agreement regarding the importance of the local structure of these materials on their oxygen storage capacity, there is a strong controversy over the coordination of Zr cations [2, 13–19]. The main purpose of the present work is to elucidate this problem.

According to the crystal structure of the tetragonal and cubic phases determined by Yashima *et al* [6], eight oxygen atoms are expected around a central Zr or Ce atom, forming two shells of four atoms in the case of the tetragonal phase or only one shell of eight atoms in the case of the cubic phase. In contrast, Vlaic *et al* [13–15] found a $4 + 2$ or $5 + 2$ oxygen shell distribution around Zr atoms for both phases, while no splitting of the first shell was found around Ce atoms. However, Lemaux *et al* [16] claimed that these $4 + 2$ or $5 + 2$ models are not correct, and indicated that a $4 + 4$ model can be obtained if the different values of the inner potential (E_0) of the two Zr–O subshells are allowed, while they were fixed equal in the works of Vlaic *et al* [13–15]. In addition, Fernández-García *et al* [17] found the Zr–O coordination changes from a $4 + 2$ model for samples with large crystallite size (>90 nm) and tetragonal lattice symmetry, to a $5 + 2$ model for samples with small crystallite size (<20 nm) and cubic lattice symmetry. In addition to the lack of agreement on the local structure of the Zr–O bonds of ZrO_2–CeO_2 solid solutions, it should be stressed that, surprisingly, in all these works, the results of XRD studies were not consistent with those of EXAFS analyses.

The present paper deals with the local structure of the metal–oxygen bond in ZrO_2–CeO_2 nanopowders synthesized by a pH-controlled nitrate–glycine gel-combustion process. This synthesis method leads to single-phased and compositionally homogeneous ZrO_2–CeO_2 solid solutions over the whole compositional range [11, 12]. In a recent synchrotron radiation x-ray diffraction (SR-XRD) study [12], we investigated the crystal structure of these materials. The t'/t'' and t'' /cubic compositional boundaries were determined to be (68 ± 2) and (85 ± 5) mol% CeO_2, respectively.

In the present work, the tetragonal-to-cubic transition in nanostructured ZrO_2–CeO_2 solid solutions has been investigated by Raman and x-ray absorption spectroscopies. The aim of this investigation was to confirm the tetragonal/cubic phase boundary determined by SR-XRD

and to investigate the variations of the local atomic structure around the metal ions (Zr and Ce) as a function of CeO_2 content. The main goal of this paper is to demonstrate that the tetragonal/cubic transition observed by SR-XRD in our previous study [12] is related to a tetragonal-to-cubic change in the Zr–O bond.

2. Experimental procedure

2.1. Synthesis of nanocrystalline ZrO_2–CeO_2 solid solutions

ZrO_2–15, 40, 50, 60, 65, 70, 80 and 90 mol% CeO_2 nanopowders were synthesized by a pH-controlled nitrate–glycine gel-combustion process previously developed by the authors [11, 12, 20, 21]. High-purity (99.9%) raw compounds were used. For all the compositions, the synthesis process was adjusted to obtain 5 g of the final product.

$ZrOCl_2{\cdot}8H_2O$ (Alpha Aesar, USA, 99.9%) and $Ce(NO_3)_3{\cdot}6H_2O$ (Alpha Aesar, USA, 99.9%) were dissolved in 50 ml of nitric acid (65%, Merck, Germany) in a ratio corresponding to the selected final composition and this solution was concentrated by thermal evaporation in order to eliminate chloride anions. Glycine (99%, Merck, Germany) was added in a proportion of five moles per mole of metal atom and the pH of the solution was adjusted in the range 3–7 with ammonium hydroxide (25%, Merck, Germany). The pH was tuned as close as possible to 7, taking care to avoid precipitation. The resulting solution was concentrated by evaporation using a hot plate at 200 °C until a viscous gel was obtained. This hot gel finally burnt out as a result of a vigorous exothermic reaction. The system remained homogeneous during the whole process and no precipitation was observed. Finally, the as-reacted material was calcined in air at 600 °C for 2 h in order to remove the organic residues.

The average crystallite size of the nanocrystalline powders was estimated from the width of the XRD peaks in a previous work [12]. The average size, for the different studied compositions, ranges between 8 and 20 nm.

2.2. Raman spectroscopy

Raman spectra were recorded in a Renishaw Imaging Microscope System 3000 spectrophotometer equipped with an Olympus BH-2 microscope and a CCD detector. A 632.8 nm He–Ne laser line (Spectra Physics, model 127) was used as excitation radiation and the laser power at the sample was 1.8 mW. Spectra acquisition consisted of five scans of 20 s duration each.

2.3. X-ray absorption spectroscopy

EXAFS spectra were measured at the D04B-XAFS1 beamline [22] (Brazilian Synchrotron Light Laboratory, LNLS, Campinas, SP, Brazil) in transmission mode using Si(220) and Si(110) monochromators for the Zr K edge and the Ce L_{III} edge, respectively. The nominal photon flux of the beamline is 3×10^9 photons/(s.mrad.100 mA)@6 keV. The energy range was 17 900–18 900 eV for the Zr K edge and 5690–6100 eV for the Ce L_{III} edge and it was calibrated using Zr and Cr foils, respectively. Data were collected at room temperature using energy steps of 2 eV and $E/\Delta E = 5000$–10 000. The integration time was 2 s for energies up to 18 100 eV and 4 s for higher energies. Three spectra were collected for each sample and the average spectrum was used to perform the data analysis. In the case of the ZrO_2–90 mol% CeO_2 solid solution, we used a different data collection strategy to improve the signal to noise ratio: two spectra were collected, with an energy step of 2 eV and an integration time of 10 s for energies up to 18 400 eV and an energy step of 4 eV and an integration time of 20 s for higher energies. The samples were prepared by deposition from a powder suspension in isopropanol

on a Millipore membrane. The thicknesses were adjusted to obtain a total absorption above the edge of 1.5.

In order to obtain the experimental scattering amplitudes and phases required for EXAFS data analysis, two standard compounds were used. They were $BaZrO_3$ (6 oxygen atoms at 2.09 Å) and CeO_2 (8 oxygen atoms at 2.34Å), for the Zr–O and Ce–O coordination shells, respectively. Both Debye–Waller factors were assumed to be zero (therefore, the results of these parameters are relative to their respective values in the standard compounds).

EXAFS data analysis was performed using the WINXAS code [23]. Both pre- and post-edge were subtracted from raw data. For the pre-edge region, a linear fit of the absorption signal was subtracted from the experimental data, and a fifth-order polynomial was used for the post-edge removal. In order to study the cation–oxygen bonds (first oxygen shell around Zr and Ce cations), the selected Fourier transform (FT) windows for Ce L_{III} edge analysis were 2.15–9.35 $Å^{-1}$ and 1.0–2.5 Å in reciprocal (k, wave-number) and real (R, distance to central atom) space, respectively, and, for the Zr K edge, they were 3.0–9.0 $Å^{-1}$ and 1.0–2.15 Å, respectively. A k^3-weighted oscillation was used to calculate the Fourier transform. The k window chosen for the Zr K edge was selected due to the low signal to noise ratio of EXAFS data corresponding to CeO_2-rich materials, after confirming that no significant differences were obtained with wider k windows in the case of ZrO_2-rich materials (these tests were also used to evaluate the errors in the EXAFS fitting parameters: 10% in the coordination numbers and 0.01 Å in the Zr–O distances). For the Ce L_{III} edge, it was not possible to choose a higher upper limit of the k window because of the presence of the Ce L_{II} edge.

The coordination number (CN), bond length (R), Debye–Waller factor (σ) and inner potential shift (ΔE_0) were used as free parameters in the fitting procedure. The quantitative fitting was performed only on the back Fourier transformed first shell peak. According to Vlaic and co-workers [13–15], the values of E_0 and σ were considered to be equivalent for the two different Zr–O subshells. For the Ce edge, all parameters were set free. In addition, Lemaux *et al* [16] model of EXAFS fitting was performed for the sake of comparison.

The results of the above first Zr–O shell EXAFS analysis, determined using experimental scattering amplitudes and phases (obtained from standard compounds), were compared with those determined using theoretical amplitudes and phases calculated by means of the FEFF8 code [24]. The same procedure allowed us to investigate the next nearest neighbours (NNNs) to Zr (first cation shell around Zr). This study was possible only for the Zr K-edge because of the small k-range that could be measured in the case of the Ce L_{III} edge. The selected FT windows were 3.0–12.0 $Å^{-1}$ and 1.0–4.0 Å in k- and R-space, respectively. The quantitative fitting was performed with a k^3-weighted oscillation using the FEFFIT code [25].

For the EXAFS analysis of the second coordination shell of Zr, we considered two Zr, one Ce and three O subshells (the fourth oxygen subshell expected for the tetragonal phase was not considered because it is very far from the absorber Zr atom). The coordination numbers of the cations were varied, but the sum was kept equal to 12, the expected value according to the crystal structures of the tetragonal and cubic phases. For the O subshells, the expected crystallographic coordination numbers were fixed. These third shell oxygen atoms were used during simulation to improve Zr and/or Ce CN determination, which can be affected by destructive or constructive interference among second and third shell paths. All the distances (Zr–Zr1, Zr–Zr2, Zr–Ce, Zr–O1, Zr–O2 and Zr–O3) were correlated using a crystallographic model based on the cell parameters, a and c, and the fractional z-coordinate of the O^{2-} anion in the asymmetric unit of the tetragonal unit cell, $z(O)$. The Debye–Waller factors were kept equal for equal atoms, so three parameters were included. The inner potential shift was considered to be equal for all the subshells. In this way, it was possible to reduce the number of independent variables.

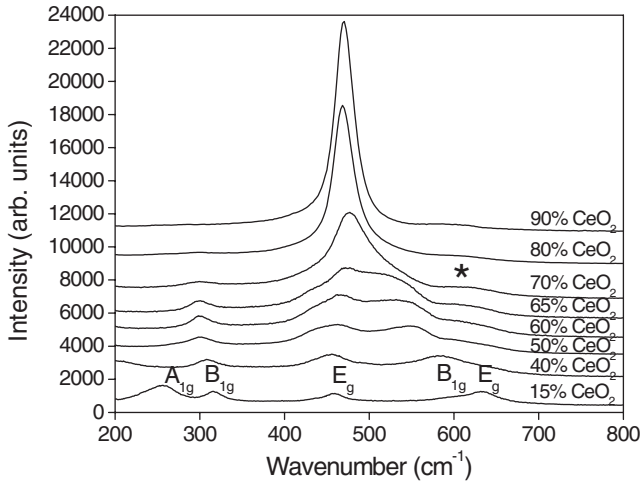

Figure 1. Raman spectra obtained for ZrO_2–15, 40, 50, 60, 65, 70, 80 and 90 mol% CeO_2 solid solutions.

3. Results

3.1. Raman spectroscopy

Raman spectroscopy was used to identify the tetragonal and cubic phases. The tetragonal phase ($P4_2/nmc$ space group) exhibits six Raman-active modes (one A_{1g}, three E_g and two B_{1g} modes), while the cubic phase ($Fm3m$ space group) only presents one F_{2g} Raman-active mode [5, 26]. In the case of the t'' form, it has been reported that some modes of the tetragonal phase are not detected [5].

Figure 1 shows Raman spectra obtained for ZrO_2–CeO_2 solid solutions containing from 15 to 90 mol% CeO_2. It can be clearly observed that ZrO_2–15 mol% CeO_2 nanopowders exhibit the five bands of the tetragonal phase expected for the wavenumber range studied in this work (one E_g mode is not observed since it has a wavenumber lower than 200 cm^{-1}). As the CeO_2 content increases, the Raman spectra and band positions changed continuously, resulting in only one band at 470 cm^{-1} in the case of the ZrO_2–90 mol% CeO_2 solid solution, which corresponds to the F_{2g} mode of the cubic phase. An extra band, marked with an asterisk in figure 1, is detected for CeO_2-rich materials, which is due to a defect structure occurring by the substitution of Zr by Ce cations [5]. The band positions are in good agreement with those reported by Yashima *et al* for ZrO_2–CeO_2 solid solutions with similar compositions [5]. The Raman spectra of samples with CeO_2 content up 80 mol% exhibit the B_{1g} mode of the tetragonal phase (at about 300 cm^{-1}), while this mode is not detected in ZrO_2–90 mol% CeO_2 (see figure 2). Therefore, the tetragonal/cubic compositional boundary is at (85 ± 5) mol% CeO_2, in agreement with our previous SR-XRD study [12].

3.2. Zr K edge EXAFS analysis

The x-ray absorption spectra and EXAFS raw data of some selected samples on the Zr K edge are shown in figures 3 and 4, respectively. As can be observed, a good signal to noise ratio was obtained up to 12 $Å^{-1}$.

The FTs of the EXAFS functions (without phase corrections) corresponding to ZrO_2–CeO_2 samples with different CeO_2 contents, at the Zr K edge, are shown in figure 5. The FTs exhibit

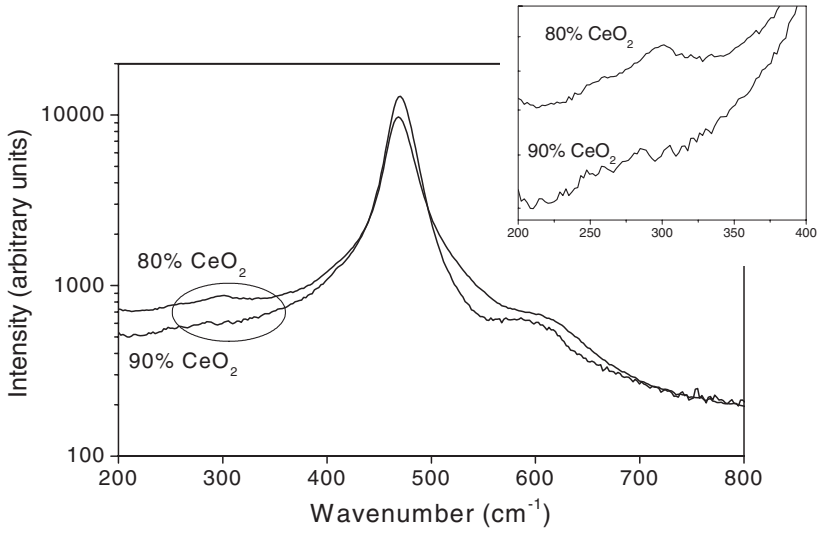

Figure 2. Raman spectra of ZrO_2–80 and 90 mol% CeO_2 solid solutions and detail of the wavenumber region close to the B_{1g} mode of the tetragonal phase.

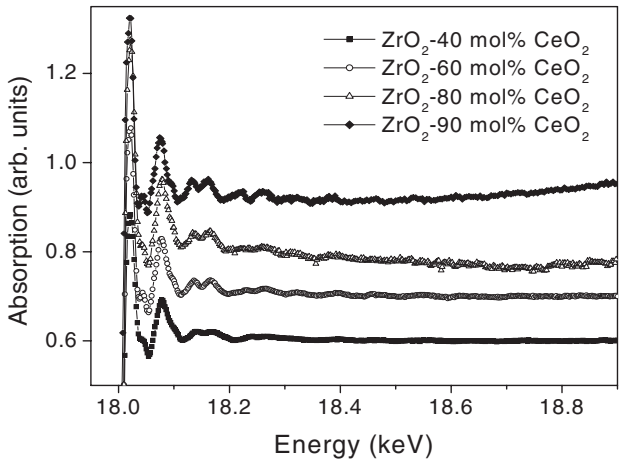

Figure 3. X-ray absorption spectra corresponding to ZrO_2–40, 60, 80 and 90 mol% CeO_2 solid solutions at the Zr K edge.

two main peaks: the first and most prominent corresponds to the Zr–O nearest neighbour shell, while the second is a superposition of Zr–cation (Zr–Zr and Zr–Ce) and second Zr–O coordination shells.

3.2.1. First coordination shell. The amplitude of the first FT peak in figure 5 exhibits a progressively increasing trend for increasing CeO_2 content. This effect may be qualitatively explained as a consequence of an increase in the coordination number (CN) or, alternatively, as a decrease in structural disorder. The shift in the position of the peak Zr–O suggests a monotonic increase in the Zr–O distance for increasing CeO_2 content.

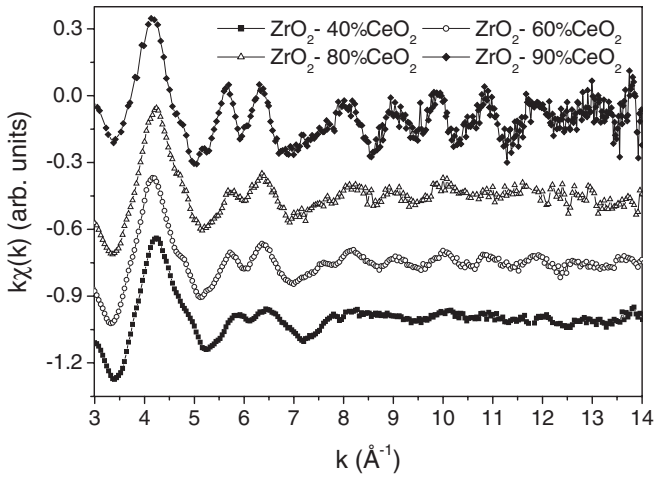

Figure 4. *k*-weighted raw EXAFS data corresponding to ZrO_2–40, 60, 80 and 90 mol% CeO_2 solid solutions at the Zr K edge.

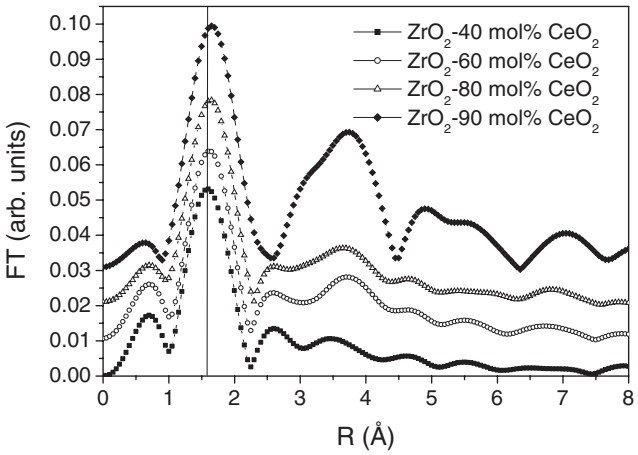

Figure 5. Fourier transforms of the EXAFS functions corresponding to ZrO_2–40, 60, 80 and 90 mol% CeO_2 solid solutions at the Zr K edge.

Several authors have established that a good EXAFS fitting for oxygen nearest neighbour atoms, at the Zr K edge, can be attained by using two subshells with different distances and CNs [13–16]. Hereafter, these two subshells will be called Zr–O1 and Zr–O2. As mentioned in the section 1, two different models have been proposed: in the Vlaic *et al* model [13–15], ΔE_0 and σ are assumed to be the same for both Zr–O subshells; in contrast, Lemaux *et al* [16] proposed that each subshell contains a fixed number of oxygen atoms equal to four, but different values of σ and ΔE_0.

In the present work, EXAFS analyses at the Zr K edge of a few selected samples were performed using both the Vlaic *et al* and Lemaux *et al* models. Both led to statistically identical results, as tested by an F-test with a 99% confidence level, and with similar quality of fit (see figure 6). The Zr–O2 distance obtained by the Vlaic *et al* model resulted in being close to the cation–O2 distance determined from SR-XRD data [12] (see table 1), while the distance

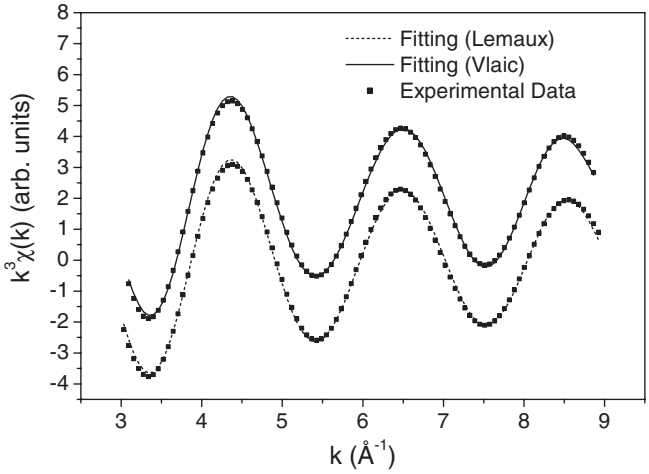

Figure 6. Back Fourier transform of k^3-weighted EXAFS spectra of the first shell for ZrO_2–15 mol% CeO_2 sample at the Zr K edge and the corresponding fit, obtained using the Vlaic *et al* and Lemaux *et al* models (see text).

Table 1. Results of the EXAFS analysis of the first coordination shell at the Zr K edge for ZrO_2–15 mol% CeO_2 nanopowders using the models proposed by Vlaic *et al* [13–15] and Lemaux *et al* [16]. Crystallographic data determined by SR-XRD [12] are also presented. CN: coordination number; R: Zr–oxygen distance (cation–oxygen distance in the case of SR-XRD); σ: Debye–Waller factor; ΔE_0: inner potential shift; χ: goodness of fit (WinXAS).

Model	CN	R (Å)	σ (Å)	ΔE_0 (eV)	χ
Lemaux *et al* [16]	4	2.08(1)	0.047(2)	0.79(8)	5.8
	4	2.29(1)	0.13(1)	−1.8(2)	
Vlaic *et al* [13–15]	4.6(5)	2.09(1)	0.061(3)	−0.45(4)	5.2
	2.0(2)	2.37(1)			
Crystallographic data [12]	4	2.112(3)			
	4	2.373(3)			

obtained using the Lemaux *et al* model resulted in being much smaller. In addition, the Debye–Waller factor of the Zr–O2 subshell obtained with this last model resulted in being unreliable, indicating that this model is not acceptable. Besides, the use of different values of ΔE_0 for equal scattering atoms located at similar distances has no chemical justification and may lead to a physically meaningless solution [14]. Consequently, we decided to analyse the first sphere of our whole set of samples using the Vlaic *et al* protocol. Following this procedure, the values of σ for both oxygen subshells were assumed to be the same, as an approximation to reduce the number of variables. It is worth mentioning that the procedure proposed by Lemaux *et al* [16] is questionable, as pointed out by Di Monte and Kaspar [2].

Table 2 summarizes the results of the EXAFS analysis using experimental scattering amplitudes and phases determined from standard compounds. The results obtained using theoretical amplitudes and phases were very similar. It can be noted that both Zr–O distances (d_{Zr-O1} and d_{Zr-O2}) increase for increasing CeO_2 content. It is also apparent that a total sevenfold coordination ($CN_{Zr-O1} + CN_{Zr-O2}$) is obtained for these samples, with CNs of about 5 and 2 for Zr–O1 and Zr–O2 subshells, respectively. In addition, the Debye–Waller factor exhibits a pronounced minima around 70 mol% CeO_2, which corresponds to the t'/t''

Table 2. Results of the EXAFS analysis of the first coordination shell at the Zr K edge for all the studied nanostructured ZrO_2–CeO_2 solid solutions using the model proposed by Vlaic *et al* [13–15]. CN: coordination number; R: Zr–oxygen distance; σ: Debye–Waller factor; ΔE_0: inner potential shift; χ: goodness of fit (WinXAS).

CeO_2 content (mol%)	CN	R (Å)	σ (Å)	ΔE_0 (eV)	χ
15	4.6(5)	2.09(1)	0.061(3)	−0.45(4)	5.2
	2.0(2)	2.37(1)			
40	5.3(5)	2.14(1)	0.060(3)	0.56(5)	3.5
	1.5(1)	2.41(1)			
50	5.4(5)	2.15(1)	0.058(3)	0.60(6)	3.0
	1.5(1)	2.42(1)			
60	5.4(5)	2.17(1)	0.0058(3)	0.67(7)	2.3
	1.7(2)	2.44(1)			
65	5.1(5)	2.16(1)	0.049(2)	0.019(2)	1.8
	1.4(1)	2.41(1)			
70	5.2(5)	2.18(1)	0.031(2)	0.43(4)	5.0
	1.7(2)	2.45(1)			
80	5.8(6)	2.16(1)	0.063(3)	0.54(5)	1.5
	1.2(1)	2.46(1)			
90	6.2(6)	2.17(1)	0.067(3)	−2.4(2)	5.8

boundary [12]. The difference between the values of ΔE_0 for different samples was not greater than two energy steps (4 eV).

3.2.2. Second coordination shell. The results obtained from the EXAFS analysis of the second shell around Zr are summarized in table 3. The total coordination number of Zr ($CN_{Zr1} + CN_{Zr2}$) and the coordination number of Ce (CN_{Ce}) are in agreement with the expected values for each composition. It can be observed that the cation–cation distances exhibit increasing trends for increasing ceria content (for an explanation of this, see section 4). The Debye–Waller factor also increases with increasing CeO_2 content.

3.3. Ce L_{III} edge EXAFS analysis

The x-ray absorption spectra and EXAFS raw data of some selected samples on the Ce L_{III} edge are shown in figures 7 and 8, respectively. The FTs of EXAFS spectra at the Ce L_{III} edge corresponding to ZrO_2–40, 60, 80 and 90 mol% CeO_2 samples are shown in figure 9. In this case, the first peak is associated to the oxygen nearest neighbours, while the second peak is a superposition of the first cation shell and the second oxygen shell around Ce.

The back-Fourier transform of the first oxygen shell of the ZrO_2–70 mol% CeO_2 sample and the corresponding fit are shown in figure 10, as an example of the good agreement obtained between them. Similar results were obtained for all compositions.

In contrast to the case of the Zr environment, there is a general agreement in the literature regarding the local structure around the Ce cation. The Ce–O bond is modeled using a single oxygen first shell (without subshells) with CN = 8. Table 4 shows our results of the fitting procedure obtained assuming one oxygen shell with a variable CN. For all the samples, the CN is indistinguishable from 8, within the error bars. The Debye–Waller factor decreases for increasing CeO_2 content, due to the fact that it was chosen as zero in pure CeO_2, the standard compound used to determine the scattering amplitude and phase shift. It exhibits a local minimum at 65 mol% CeO_2, the composition close to the t'/t'' compositional boundary [12]. As in the case of the Zr K edge, the difference between the values of E_0 for different samples was not larger than two energy steps (4 eV).

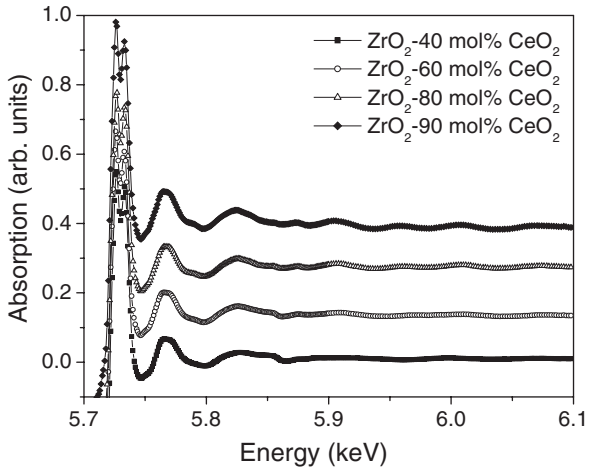

Figure 7. X-ray absorption spectra corresponding to ZrO_2–40, 60, 80 and 90 mol% CeO_2 solid solutions at the Ce L_{III} edge.

Table 3. Results of the EXAFS analysis of the second coordination shell at the Zr K edge for all the studied nanostructured ZrO_2–CeO_2 solid solutions. CN: coordination number; R: Zr–cation distance; σ: Debye–Waller factor; ΔE_0: inner potential shift; R factor: goodness of fit (FEFFIT).

CeO_2 content (mol%)	Bond	CN	R (Å)	σ (Å)	ΔE_0 (eV)	R factor (%)
15	Zr–Zr1	3.5(3)	3.62(4)	0.097(5)	2.9(3)	2.37
	Zr–Zr2	7.1(7)	3.65(4)			
	Zr–Ce	1.4(1)	3.70(4)	0.068(3)		
40	Zr–Zr1	2.1(2)	3.57(4)	0.066(3)	−0.68(7)	3.12
	Zr–Zr2	4.2(4)	3.71(5)			
	Zr–Ce	5.7(6)	3.71(5)	0.085(4)		
50	Zr–Zr1	1.8(2)	3.60	0.074(4)	1.0(1)	3.07
	Zr–Zr2	3.6(4)	3.73(5)			
	Zr–Ce	6.7(7)	3.73(5)	0.091(5)		
60	Zr–Zr1	1.5(2)	3.66(3)	0.095(5)	0.052(5)	2.72
	Zr–Zr2	3.1(3)	3.71(3)			
	Zr–Ce	7.4(7)	3.72(3)	0.085(4)		
65	Zr–Zr1	1.3(1)	3.68(3)	0.096(5)	0.30(3)	2.24
	Zr–Zr2	2.6(3)	3.73(3)			
	Zr–Ce	8.1(8)	3.74(3)	0.093(5)		
70	Zr–Zr1	1.1(1)	3.69(3)	0.110(6)	1.2(1)	2.72
	Zr–Zr2	2.2(2)	3.75(3)			
	Zr–Ce	8.7(9)	3.75(3)	0.093(5)		
80	Zr–Zr1	1.0(1)	3.70(3)	0.098(5)	0.76(8)	3.51
	Zr–Zr2	2.0(2)	3.72(3)			
	Zr–Ce	9.0(9)	3.75(3)	0.099(5)		
90	Zr–Zr	1.6(2)	3.79(3)	0.11(1)	3.5(4)	3.69
	Zr–Ce	10.4(9)	3.79(3)	0.099(5)		

4. Discussion

Our results of Raman spectroscopy confirmed the tetragonal-to-cubic phase transition for varying composition in nanostructured ZrO_2–CeO_2 solid solutions and the tetragonal (t'')/cubic

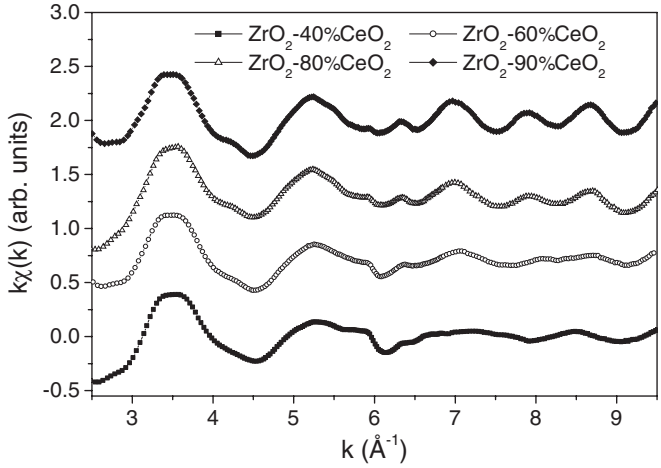

Figure 8. k-weighted raw EXAFS data corresponding to ZrO_2–40, 60, 80 and 90 mol% CeO_2 solid solutions at the Ce L_{III} edge.

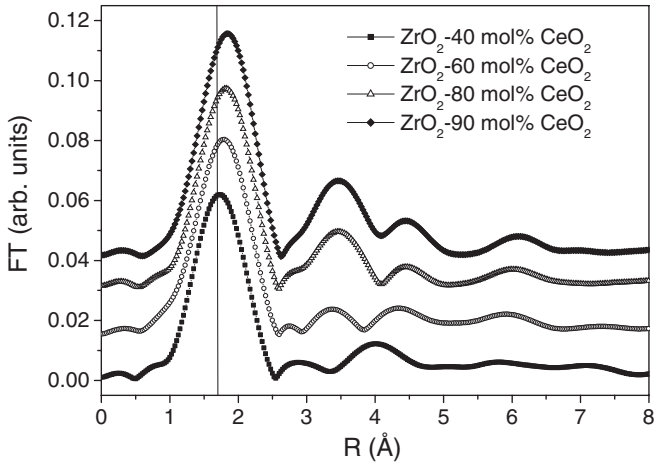

Figure 9. Fourier transforms of the EXAFS functions corresponding to ZrO_2–40, 60, 80 and 90 mol% CeO_2 solid solutions at the Ce L_{III} edge.

phase boundary (85 mol% CeO_2) determined by SR-XRD [12]. Additionally, the EXAFS analysis made possible a detailed structural characterization of the changes in the local structure as a function of the composition, below and above the phase boundaries (t'/t'' and t''/c).

The Zr–O and Ce–O distances obtained from the EXAFS analysis are summarized in tables 2 and 4, respectively. The parameters obtained from this analysis are shown in figures 11–13. In figure 11, it is apparent that both Zr–O distances exhibit increasing trends for increasing ceria content. This can be explained by considering that the ionic radius of Ce^{4+} (1.01 Å) is larger than that of Zr^{4+} (0.89 Å). As the CeO_2 content increases, the Ce–O distance moves towards the reference value of 2.34 Å, which corresponds to the value found in the cubic structure of pure CeO_2 [13–15]. This is in agreement with the tetragonal-to-cubic structural change observed at (85 ± 5) mol% CeO_2, reported in our previous SR-XRD study [12].

Our EXAFS measurements probed the average local structures around the Zr atoms and Ce atoms. On the other hand, for a substitutional solid solution such as the ZrO_2–CeO_2 materials

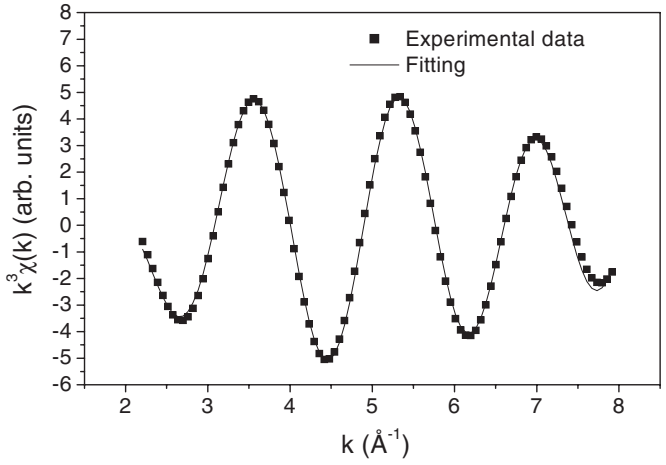

Figure 10. Back Fourier transform of k^3-weighted EXAFS spectra of the first shell for ZrO_2–70 mol% CeO_2 sample at the Ce L_{III} edge and the corresponding fit.

Table 4. Results of the EXAFS analysis of the first coordination shell at the Ce L_{III} edge for all the studied ZrO_2–CeO_2 nanopowders. CN: coordination number; R: Ce–oxygen distance; σ: Debye–Waller factor; ΔE_0: inner potential shift; χ: goodness of fit (WinXAS).

CeO_2 content (mol%)	CN	R (Å)	σ (Å)	ΔE_0 (eV)	χ
15	7.7(8)	2.26(1)	0.072(4)	−2.5(3)	16.2
40	7.3(7)	2.28(1)	0.067(3)	−2.1(2)	11.0
50	7.2(7)	2.29(1)	0.062(3)	−1.8(2)	8.3
60	7.5(7)	2.30(1)	0.058(3)	−1.1(1)	3.6
65	7.4(7)	2.31(1)	0.038(2)	−1.0(1)	4.0
70	7.5(7)	2.31(1)	0.049(2)	−0.82(8)	5.4
80	7.7(8)	2.32(1)	0.044(2)	−0.62(6)	4.9
90	7.8(8)	2.33(1)	0.028(1)	−0.30(3)	2.2

studied here, the crystal structure determined by XRD corresponds to the average of local structures over all unit cells. This is shown in figure 14. Three oxygen shells are superimposed, two corresponding to oxygen subshells around Zr (light grey) and one to the oxygen shell around Ce (dark grey). For the sake of clarity, a simple 6 + 2 coordination model has been considered for Zr. Six O atoms are located at a distance d(Zr–O1) from Zr, two O atoms are at a distance d(Zr–O2) from Zr and eight O atoms are at a distance d(Ce–O) from Ce. The averaging over the unit cells of the ZrO_2–CeO_2 solid solutions leads to two different average cation–oxygen distances, d(cation–O_i) ($i = 1; 2$). If no oxygen vacancies are present, these distance are simply the weighted averages:

$$d(\text{cation–O}_i) = d(\text{Zr–O}i)(1 - X) + d(\text{Ce–O})X \qquad (i = 1; 2) \tag{1}$$

where X is the molar fraction of Ce atoms. However, if the presence of oxygen vacancies around Zr or Ce is taken into account, the distance averaging should be modified as follows:

$$d(\text{cation–O}i) = \frac{d(\text{Zr–O}i)(1 - X)(\text{CN}^i_{\text{Zr}}/\text{CN}^i_{\text{Zr}'}) + d(\text{Ce–O})X(\text{CN}_{\text{Ce}}/\text{CN}_{\text{Ce}'})}{(1 - X)(\text{CN}^i_{\text{Zr}}/\text{CN}^i_{\text{Zr}'}) + X(\text{CN}_{\text{Ce}}/\text{CN}_{\text{Ce}'})} \qquad (i = 1; 2) \tag{2}$$

where CN^1_{Zr}, CN^2_{Zr} and CN_{Ce} are the coordination numbers determined from EXAFS analysis

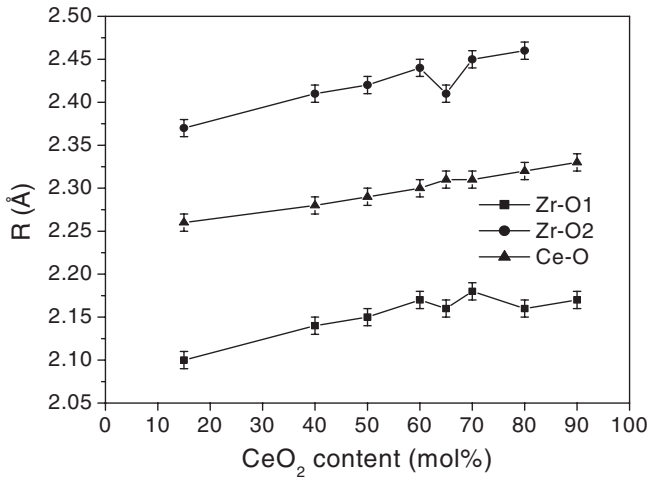

Figure 11. Zr–O1, Zr–O2 and Ce–O distances determined by EXAFS analysis of the first shell around Zr and Ce cations.

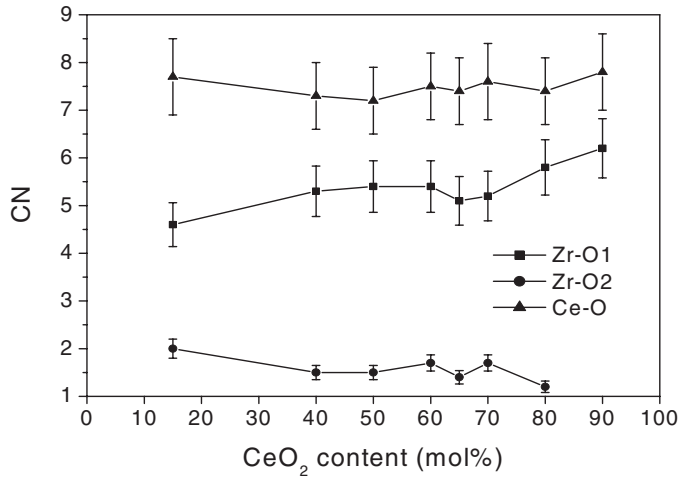

Figure 12. Coordination numbers of the Zr–O1, Zr–O2 and Ce–O bonds determined by EXAFS analysis.

and $CN^1_{Zr'}$, $CN^2_{Zr'}$ and $CN_{Ce'}$ are the corresponding values when no vacancies are present (in the case of the simple model shown in figure 14, these coordination numbers are 6, 2 and 8, respectively). Equation (2) can be expressed in a simpler form, without assuming any model for the local structure around Zr, by considering that the concentration of oxygen vacancies in both oxygen subshells around Zr is approximately equal, i.e.:

$$CN^1_{Zr}/CN^1_{Zr'} = CN^2_{Zr}/CN^2_{Zr'} = (CN^1_{Zr} + CN^2_{Zr})/(CN^1_{Zr'} + CN^2_{Zr'}) = CN_{Zr}/8 \qquad (3)$$

where CN_{Zr} is the total coordination number of Zr and it has been assumed that $CN^1_{Zr'} + CN^2_{Zr'}$ is equal to 8, the expected crystallographic coordination of Zr. With this approximation and using $CN_{Ce'} = 8$, equation (2) can be rewritten as

$$d(\text{cation–O}i) = \frac{d(\text{Zr–O}i)(1-X)(CN_{Zr}/8) + d(\text{Ce–O})X(CN_{Ce}/8)}{(1-X)(CN_{Zr}/8) + X(CN_{Ce}/8)} \qquad (i = 1; 2). \qquad (4)$$

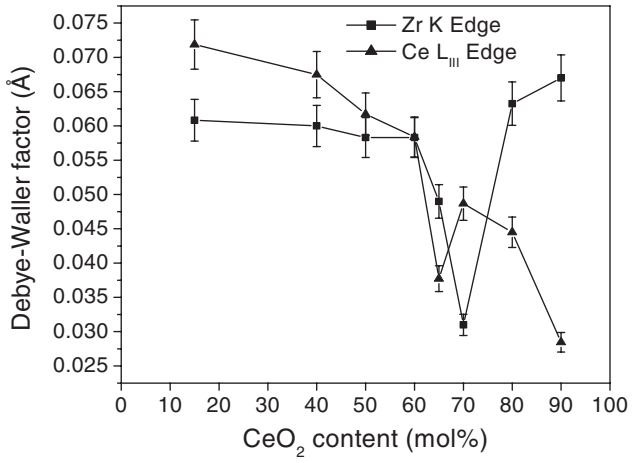

Figure 13. Debye–Waller factor of the Zr–O (considered equal for Zr–O1 and Zr–O2, see text) and Ce–O bonds determined by EXAFS analysis.

Table 5. Average cation–oxygen distances determined from the results of EXAFS analysis compared to SR-XRD data.

	Averaged EXAFS data		SR-XRD data	
CeO_2 content (mol%)	*d* (cation–O1) (Å)	*d* (cation–O2) (Å) (Å)	*d* (cation–O1) (Å) (Å)	*d* (cation–O2) (Å) (Å)
15	2.13(2)	2.35(2)	2.112(3)	2.372(3)
40	2.20(2)	2.36(2)	2.185(3)	2.361(3)
50	2.22(2)	2.35(2)	2.211(3)	2.358(3)
60	2.25(2)	2.35(2)	2.243(6)	2.347(6)
65	2.26(2)	2.34(2)	2.256(6)	2.348(6)
70	2.27(2)	2.35(2)	2.265(9)	2.351(9)
80	2.29(2)	2.35(2)	2.29(1)	2.35(1)
90	2.32(2)		2.330(2)	

As shown in table 5 and figure 15, the *d*(cation–O1) and *d*(cation–O2) distances obtained from EXAFS results using equation (4) agree very well with those independently determined from SR-XRD data [12] using the simple expressions

$$d(\text{cation–O1}) = [0.125 * a^2 + (z(\text{O}) * c)^2]^{1/2} \tag{5a}$$

$$d(\text{cation–O2}) = [0.125 * a^2 + (0.5 - z(\text{O}))^2 * c^2]^{1/2} \tag{5b}$$

where a and c are the lattice parameters and z(O) is the fractional z-coordinate of the oxygen atom in the asymmetric unit.

It is worth mentioning that EXAFS measures a unidimensional average of instantaneous interatomic distances for each coordination shell of the absorber atom [27, 28]. Therefore, the average interatomic distance determined from EXAFS analysis is generally slightly larger than the real one, due to the effect of the thermal vibrations normal to the bond direction [27]. Since this effect is only appreciable at high temperatures [28], it can be neglected in the present case. However, structural disorder could also introduce differences between the average distances determined by EXAFS and XRD analyses.

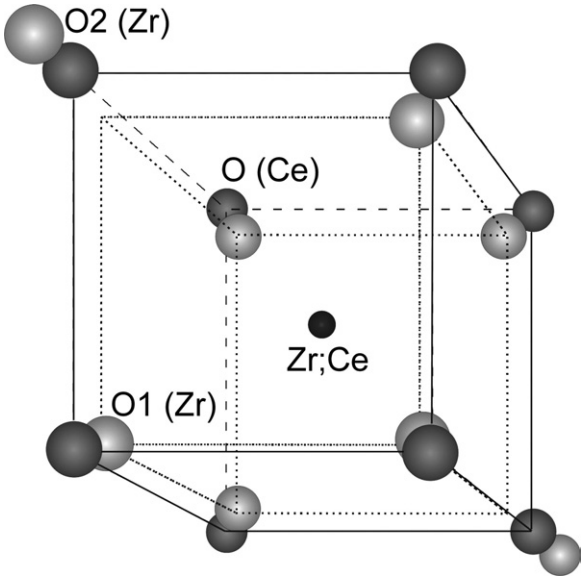

Figure 14. Schematic representation of the average crystal structure of a substitutional ZrO_2–CeO_2 solid solution. The oxygen shells around Zr (6 + 2 coordination model) and Ce are marked in light and dark grey, respectively. The different size of oxygen anions is only due to the perspective of the figure.

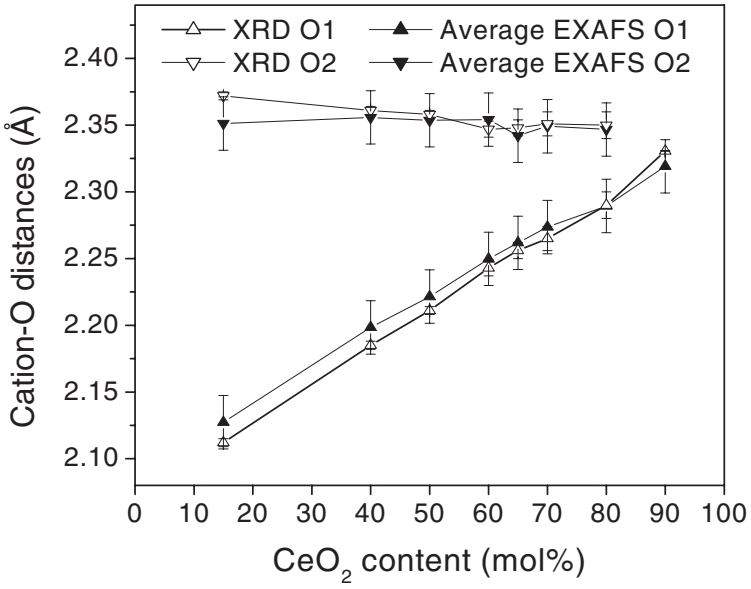

Figure 15. Comparison between the average cation–O1 and cation–O2 distances determined from the results of EXAFS analysis and those obtained by SR-XRD.

Ce–O, Zr–O1 and Zr–O2 coordination numbers resulted in being almost independent over the composition range between 40 and 80 mol% CeO_2 (see tables 2 and 4 and figure 12). The coordination of Ce was determined to be eightfold, as expected according to the crystal

structure of ZrO_2–CeO_2 solid solutions (tetragonal or cubic). This was not the case of the Zr local environment, for which a sevenfold coordination was determined for all the compositions exhibiting the tetragonal phase. For the sample with the highest CeO_2 concentration—ZrO_2–90%molar CeO_2—the results of EXAFS analysis exhibit clear differences as compared to those of lower CeO_2 content, with tetragonal structure. In fact, only a single Zr–O distance was detected and the coordination number (CN $\approx$ 6) resulted in being lower than the total coordination of the oxygen first shell of samples with tetragonal structure (CN $\approx$ 7). Thus, the tetragonal-to-cubic transition observed by SR-XRD in the previous study mentioned [12] is related to a tetragonal-to-cubic change in the Zr–O bond.

Sevenfold coordination of Zr has been reported for cubic ZrO_2–Y_2O_3 solid solutions by Li and co-authors [29]. They attributed this coordination to the presence of vacancies (introduced by Y^{3+} cations), which are preferentially located as nearest neighbours of Zr. However, this argument is not applicable to the tetragonal phase, since a low Y_2O_3 content is required to retain the tetragonal phase, thus reducing the concentration of vacancies. For this reason, the authors considered (somewhat arbitrarily) that the coordination of Zr is eightfold in these materials [29]. Taking into account that their EXAFS results—derived under this assumption—did not accord with the long-range order derived by XRD [29], the eightfold coordination model proposed by Li *et al* for the Zr cation in tetragonal Y_2O_3-doped ZrO_2 solid solutions is prone to criticism.

In the case of the ZrO_2–CeO_2 solid solutions, the presence of vacancies is not expected, since Ce cations have a 4+ valence state (nevertheless, the presence of Ce^{3+} cannot be ruled out). Thus the sevenfold coordination of Zr cations—established in the present investigation—should be assigned to other causes. It must be taken into account that a rather high number of vacancies are expected to be formed in the studied system as a consequence of the inherent high structural disorder of nanostructured materials. In order to confirm that vacancies induced by structural disorder are responsible for the observed sevenfold coordination of Zr cations, additional investigations are required.

On the other hand, it is well known that the strong covalent nature of Zr–O bonding in the ZrO_2 lattice promotes the sevenfold coordination [30], as observed in monoclinic ZrO_2. Therefore, it is possible that the Zr also exhibits this coordination in the tetragonal phase. To our knowledge, this possibility has not been carefully considered until now.

The Debye–Waller factors (σ) associated to the oxygen first shell around Zr and Ce are displayed in figure 13 as functions of composition. A pronounced local minimum for CeO_2 contents between 65 and 70 mol% in both Zr and Ce environments can be noticed. This composition range corresponds to the boundary between the t' and t'' metastable tetragonal forms (68 mol% CeO_2 [12]). The relevance and explanation of this result require additional and careful EXAFS analyses of several samples with compositions close to this phase boundary.

The Zr–Zr and Zr–Ce distances obtained from the EXAFS analysis of the first cation shell around Zr are summarized in tables 3 and shown in figure 16. As in the case of the cation–oxygen distances, all the Zr–cation distances increase with increasing ceria content due to the larger ionic radius of Ce^{4+} compared to that of Zr^{4+}. The small difference between all the Zr–cation distances for CeO_2 contents higher than 60 mol% is related to the t'/t'' transition. In our previous SR-XRD study [12], we found that the t'/t'' compositional boundary is at (68 $\pm$ 2) mol% CeO_2.

From the results of table 3, it can be observed that the Debye–Waller of the NNNs to Zr increases with increasing CeO_2 content. This is possible due to a distortion of the Zr sublattice caused by the incorporation of Ce considering the ionic radii mismatch between them.

Finally, figure 17 depicts an important compatibility between the local structure model and experimental data. It displays the CeO_2 content deduced from the EXAFS analysis of the NNNs to Zr as a function of the nominal composition. A very good agreement can be

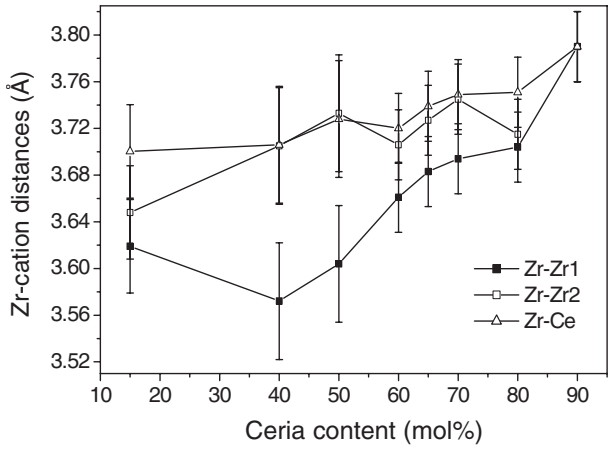

Figure 16. Zr–Zr1, Zr–Zr2 and Zr–Ce distances determined by EXAFS analysis of the metal neighbours of Zr.

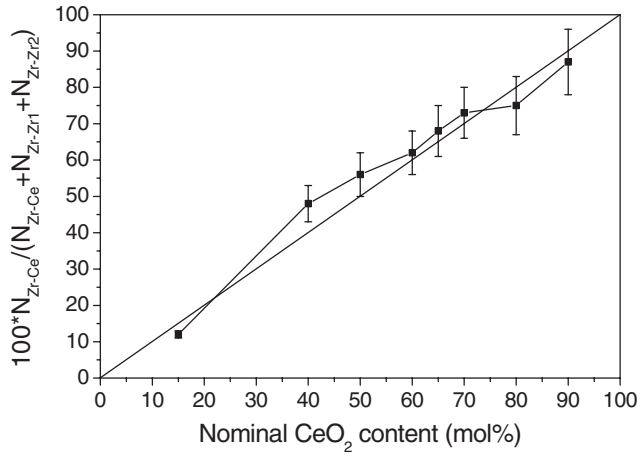

Figure 17. Comparison between nominal composition and the composition calculated from the coordination numbers determined by EXAFS analysis of the metal neighbours of Zr.

observed, indicating that the synthesis method yields highly homogeneous samples. Even though the compositional homogeneity of powders synthesized by gel-combustion routes is well known (see, for example, [12] and references therein), this information is relevant since it demonstrates the homogeneity at an atomic level, which is very important for the oxygen storage/release capacity of ZrO_2–CeO_2 materials [19].

5. Concluding remarks

Compositionally homogeneous ZrO_2–CeO_2 nanopowders synthesized by a pH-controlled nitrate–glycine gel-combustion route have been studied by Raman and EXAFS spectroscopies. The tetragonal/cubic compositional phase boundary derived by both techniques was of (85 ± 5) mol% CeO_2, in agreement with a previous SR-XRD study [12].

EXAFS analysis demonstrates that the tetragonal-to-cubic compositional transition is related to a symmetry change of the oxygen first shell around Zr cations, from two subshells

and CN $\approx$ 7 in the tetragonal phase towards a single shell and CN $\approx$ 6 in the cubic phase. All bond lengths exhibit an increasing trend over the whole concentration range.

The present investigation evidences an excellent agreement, over the whole compositional range, between the first neighbour distances revealed by EXAFS and the average cation–oxygen distances determined from our previous SR-XRD data [12]. This clear agreement demonstrates the robustness of the model derived from EXAFS data. It should be noticed that this consistency of XRD and EXAFS results was not established in the other previous studies dealing with nanostructured ZrO_2–CeO_2 solid solutions [13–19]. The same discrepancy has been found by Li *et al* in ZrO_2–Y_2O_3 solid solutions [26].

The coordination of Zr and Ce cations was determined to be sevenfold and eightfold, respectively, for all solid solutions exhibiting the tetragonal phase (i.e., CeO_2 contents up to 80 mol%). The sample with a CeO_2 content of 90 mol%—corresponding to the cubic phase—exhibits a single shell with a coordination number close to 6. Thus, the coordination of Zr atoms were found to be, for all concentrations, lower than the value expected for a perfect solid solution (CN $=$ 8). This effect cannot be simply explained as a surface effect related to the nanometric sizes of the studied crystals. Even though it can be assigned to the presence of a high number of vacancies inside the nanocrystals, it could be also due to a general feature of the Zr–O bonding in ZrO_2-based solid solutions, independently of the phase or the crystallite size, since its strong covalent nature promotes the sevenfold coordination of Zr [27]. In fact, the above-mentioned disagreement between XRD and EXAFS results clear shows that the local environment of Zr in ZrO_2-based materials is not fully understood yet and, therefore, this possibility deserves a deep investigation.

A surprising finding, that will be pursued in the future, was the significant decrease in the Debye–Waller factor observed at concentrations corresponding to the t'/t'' boundary.

Finally, the EXAFS analysis of the first Zr–cation shell demonstrates that the studied ZrO_2–CeO_2 nanopowders are compositional homogeneous at an atomic level, which is very important for applications in three-way catalysis.

Acknowledgments

The present work was performed within the frame of the scientific collaboration agreements CAPES-SECyT and CNPq-CONICET between Brazil and Argentina. It was also partially supported by LNLS (Brazilian Synchrotron Light Laboratory, Brazil, proposal D04B-XAFS1-1868), CNPq (Brazil, PROSUL program), Agencia Nacional de Promoción Científica y Tecnológica (Argentina, PICT No. 8688 and PICT 14268), CONICET (Argentina, PIP No. 6559), Fundación YPF (Argentina, Repsol YPF Award 2003) and Fundación Antorchas (Argentina, project 14116-50).

References

[1] Trovarelli A 2002 *Catalysis by Ceria and Related Materials* (London: Imperial College Press)
[2] Di Monte R and Kaspar J 2005 *J. Mater. Chem.* **15** 633
[3] Yashima M, Morimoto K, Ishizawa N and Yoshimura M 1993 *J. Am. Ceram. Soc.* **76** 1745
[4] Yashima M, Morimoto K, Ishizawa N and Yoshimura M 1993 *J. Am. Ceram. Soc.* **76** 2865
[5] Yashima M, Arashi H, Kakihana M and Yoshimura M 1994 *J. Am. Ceram. Soc.* **77** 1067
[6] Yashima M, Sasaki S, Yamaguchi Y, Kakihana M, Yoshimura M and Mori T 1998 *Appl. Phys. Lett.* **72** 182
[7] Yashima M, Ohtake K, Kakihana M and Yoshimura M 1994 *J. Am. Ceram. Soc.* **77** 1869
[8] Yashima M, Ohtake K, Kakihana M and Yoshimura M 1994 *J. Am. Ceram. Soc.* **77** 2773
[9] Luo M F, Lu G L, Zheng X M, Zhong Y L and Wu T H 1998 *J. Mater. Sci. Lett.* **17** 1553
[10] Kaspar J, Fornasiero P, Balducci G, Di Monte R, Hickey N and Sergo V 2003 *Inorg. Chim. Acta* **349** 217

[11] Lamas D G, Lascalea G E, Juárez R E, Djurado E, Pérez L and Walsöe de Reca N E 2003 *J. Mater. Chem.* **13** 904
[12] Lamas D G, Fuentes R O, Fábregas I O, Fernández de Rapp M E, Lascalea G E, Casanova J R, Walsöe de Reca N E and Craievich A F 2005 *J. Appl. Crystallogr.* **38** 867
[13] Vlaic G, Fornasiero P, Geremia S, Kaspar J and Graziani M 1997 *J. Catal.* **168** 386
[14] Vlaic G, Di Monte R, Fornasiero P, Fonda E, Kaspar J and Graziani M 1999 *J. Catal.* **182** 378
[15] Fornasiero P, Fonda E, Di Monte R, Vlaic G, Kaspar J and Graziani M 1999 *J. Catal.* **187** 177
[16] Lemaux S, Bensaddik A, van der Eerden A M J, Bitter J H and Koningsberger D C 2001 *J. Phys. Chem.* B **105** 4810
[17] Conesa J C, Fernández-García M and Martínez-Arias A 2002 *Catalysis by Ceria and Related Materials* ed A Trovarelli (London: Imperial College Press) p 204
[18] Nagai Y, Yamamoto T, Tanaka T, Yoshida S, Nonaka T, Okamoto T, Suda A and Sugiura M 2001 *J. Synchrotron Radiat.* **8** 616
[19] Nagai Y, Yamamoto T, Tanaka T, Yoshida S, Nonaka T, Okamoto T, Suda A and Sugiura M 2002 *Catal. Today* **74** 225
[20] Lamas D G, Juárez R E, Lascalea G E and Walsöe de Reca N E 2001 *J. Mater. Sci. Lett.* **20** 1447
[21] Lascalea G E, Lamas D G, Pérez L, Cabanillas E D and Walsöe de Reca N E 2004 *Mater. Lett.* **58** 2456
[22] Tolentino H C N, Cezar J C, Compagnon-Cailhol V, Tamura E and Alves M C M 1998 *J. Synchrotron Radiat.* **5** 521
[23] Ressler T 1998 *J. Synchrotron Radiat.* **5** 118
[24] Ankudinov A L, Ravel B, Rehr J J and Conradson S D 1998 *Phys. Rev.* B **58** 7665
[25] Newville M, Ravel B, Haskel D, Rehr J J, Stern E A and Yacoby Y 1995 *Physica* B **208/209** 154
[26] Keramidas V G and White W B 1974 *J. Am. Ceram. Soc.* **57** 22
[27] Dalba G and Fornasini P 1997 *J. Synchrotron Radiat.* **4** 243
[28] Filipponi A and Di Cicco A 1995 *Phys. Rev.* B **51** 12322
[29] Li P, Chen I-W and Penner-Hahn J E 1993 *Phys. Rev.* B **48** 10074
[30] Ho S M 1982 *Mater. Sci. Eng.* **54** 23